Supporting Information

Preparation, Electrical and Electrochemical Characterizations of CuCoNiFeMn High-Entropy-Alloy for Overall Water Splitting at Neutral-pH

Arumugam Sivanantham,[a,b] Hansung Lee,[a,b] Sung Won Hwang,[a,b] Byungmin Ahn,[a,b,*]

In Sun Cho[a,b,*]

[a]Department of Materials Science & Engineering, Ajou University, Suwon 16499, South Korea

[b]Department of Energy Systems Research, Ajou University, Suwon 16499, South Korea

Corresponding Author's emails: byungmin@ajou.ac.kr (BA), insuncho@ajou.ac.kr (ISC)

Table S1. Purity and particle size of elemental powders used for HEA synthesis.

Element	**Cu**	**Co**	**Fe**	**Ni**	**Mn**
Purity (%)	>99.5	>99.7	>99.5	>99.7	>99.5
Particle size (μm)	<45	2~3	<45	<5	<45

Table S2. Calculation of thermodynamic parameters of δ, ΔH, ΔS, Ω, Δχ and VEC.

Parameters	Fe	Co	Ni	Mn	Cu	HEA
C_i (at.%)	5	20	20	35	20	100
C_i fraction	0.05	0.2	0.2	0.35	0.2	1
Radius-r_i (pm)	126	125	124	127	128	-
Radius-r* (pm)	-					126.15
δ (%)	-					2.25
X	1.83	1.88	1.91	1.55	1.9	1.75
Δχ	-					0.062
VEC	8	9	10	7	11	8.85
ΔS_{mix} (J/mol*K)	1.25	2.68	2.68	3.05	2.68	12.34
T_m (K)	1811	1768	1726	1519	1358	
ΔH_{mix} (kJ/mol)	-					-0.52
Ω	-					2.81

Table S3. Calculation of thermodynamic parameter of ΔH_{mix} (kJ/mol).

ΔH_{mix} (kJ/mol)	Fe-Co	F-Ni	Fe-Mn	Fe-Cu	Co-Ni	Co-Mn
	-0.04	-0.08	0	0.52	0	-1.4
	Co-Cu	Ni-Mn	Ni-Cu	Mn-Cu	Total = ΣH_{ij}	
	0.96	-2.24	0.64	1.12	-0.52	

Table S4. Summary of calculated thermodynamic parameters towards single phase HEA formation.

Parameter	Equations	For single-phase (criteria)
VEC	$VEC = \sum_{i=1}^{n} c_i VEC_i$	≥ 8 (FCC)
Atomic size difference	$\delta = \sqrt{\sum_{I=1}^{n} c_i \left(1 - \frac{r_i}{r}\right)^2} \times 100 \quad , \quad r = \sum_{i=1}^{n} c_i r_i$	δ≤6.6% (single phase)
Enthalpy of mixing	$\Delta H_{mix} = 4 \sum_{i=1,\ i \neq j}^{n} \Delta H_{ij}^{mix} c_i c_j$	
Entropy of mixing	$\Delta S_{mix} = -R \sum_{i=1}^{n} c_i \ln c_i$	

Omega parameter (Interaction parameter)	$\Omega = \frac{T_m \Delta S_{mix}}{\lvert \Delta H_{mix} \rvert} = \frac{\sum_{i=1}^{n} c_i (T_m)_i \times \Delta S_{mix}}{\lvert \Delta H_{mix} \rvert}$, $T_m = \sum_{i=1}^{n} c_i (T_m)_i$	Ω ≥ 1.1 (single phase)
Electronegativity difference	$\Delta\chi = \sqrt{\sum_{I=1}^{n} c_i (\chi_i - \chi)^2}$, $\chi = \sum_{i=1}^{n} c_i \chi_i$	For 1%<δ<6%; Δχ <0.118 (single phase)

Table S5. Different metal contents in the HEA-60h electrode before and after stability tests analyzed with ICP-OES.

CuCoNiFeMn	*Cu (at%)*	*Co (at%)*	*Ni (at%)*	*Fe (at%)*	*Mn (at%)*
Fresh electrode	22.47	21.06	21.73	6.99	34.20
After HER stability	22.26	20.82	21.67	6.98	33.97
After OER stability	21.74	20.23	20.89	6.83	32.73

Table S6. Comparison of stability (duration time) of bulk HEA with other reported HEA and non-HEA nanostructured electrocatalysts in acid (0.5 M H_2SO_4), neutral (1 M PBS) and alkaline electrolyte (1 M KOH).

Catalysts	Electrochemical oxygen and hydrogen evolution stability in (time in hours)						Ref.
	Acid pH		Neutral pH		Alkaline pH		
	OER	HER	OER	HER	OER	HER	
HEA[a] (CuCoNiFeMn)	**NA**	**10**	**15**	**20**	**10**	**20**	**This work**
Ni-S-Se[bc]	NA	NA	20	20	NA	NA	[1]
MnFeCoNiCu[b]	NA	NA	NA	NA	24	NA	[2]
$(CoCuFeMnNi)_3O_4$[b]	NA	NA	NA	NA	12	NA	[3]
FeNiMnCrCu[b]	NA	NA	NA	NA	10	NA	[4]
FeCoNiCrNbO[b]	NA	NA	NA	NA	30	NA	[5]
np-AlNiCoFeMo[b]	NA	NA	NA	NA	50	NA	[6]
CoFeLaNiPt[b]	NA	NA	NA	NA	1	1	[7]
MnCoNiFe[b]	NA	NA	NA	NA	20	NA	[8]
HF-CoCrFeNiAl[a]	NA	NA	NA	NA	10	NA	[9]
PtAuPdRhRu[b]	NA	NA	NA	NA	NA	8	[10]
$Pt_{18}Ni_{26}Fe_{15}Co_{14}Cu_{27}/C$[b]	NA	NA	NA	NA	NA	10	[11]
FeCoNiAlTi[a]	NA	NA	NA	NA	NA	40	[12]

a – bulk; b – nano; c – non-HEA; NA – not

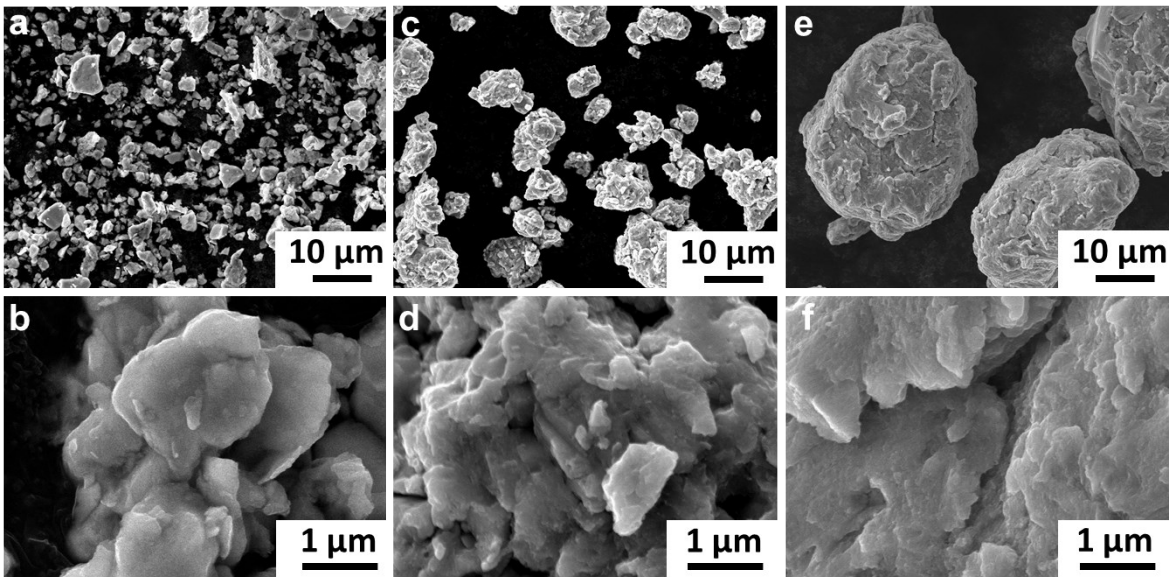

Fig. S1. Morphology of HEA: Low and high magnification SEM images of (a,b) MMP-1h. (c,d) MPA-15h. (e,f) HEA-60h.

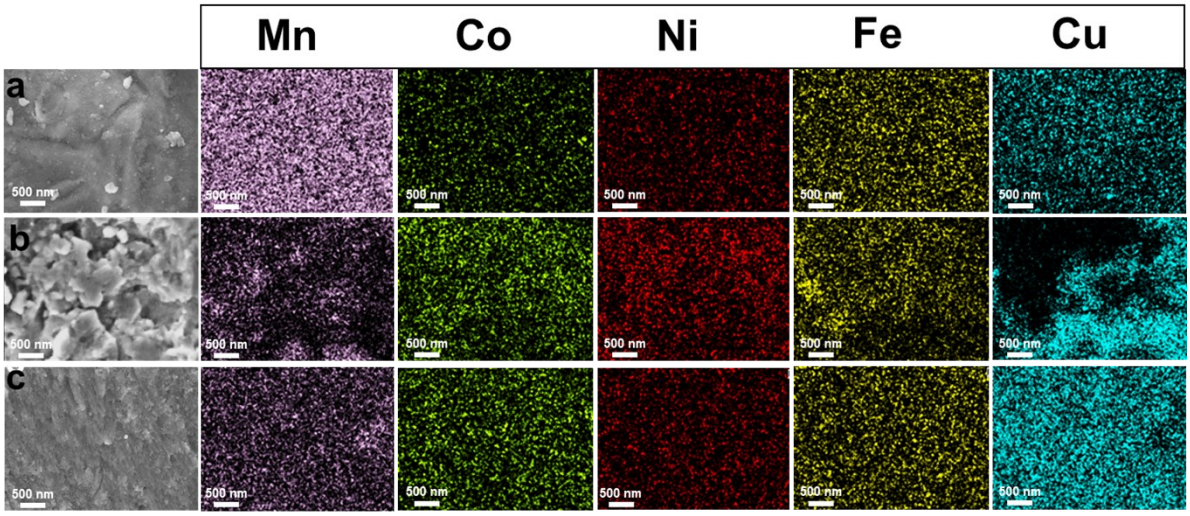

d

Element	*Atomic %*		
	MMP-1h	*MPA-15h*	*HEA-60h*
Cu	0.7	16.6	18.6
Co	2.2	28.4	19.1
Ni	1.2	21.9	19.7
Fe	1.2	9.2	7.7
Mn	95.5	23.8	34.9

Fig. S2. Nanoscale elemental mapping of HEA: Distribution of elements at high magnification-scanning electron microscopy of (a) MMP-1 h. (b) MPA-15 h. (c) HEA-60 h.

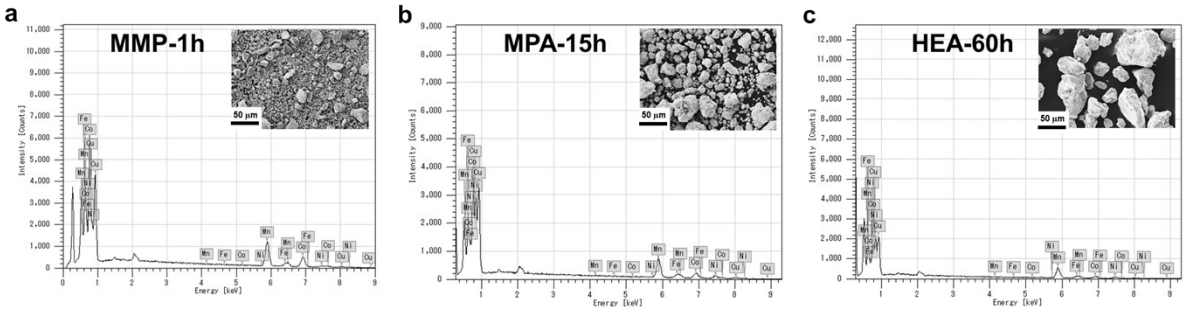

d

CuCoNiFeMn	*Cu (at%)*	*Co (at%)*	*Ni (at%)*	*Fe (at%)*	*Mn (at%)*
Precursor amount	20	20	20	5	35
MMP-1h	18.92	34.75	5.82	4.05	36.47
MPA-15h	21.74	20.90	19.51	6.72	31.13
HEA-60h	20.58	17.00	17.80	7.85	36.77

Fig. S3. Elemental quantification (atomic%) of HEA: Energy dispersive spectra-scanning electron microscopy (EDS-SEM) of (a) MMP-1h. (b) MPA-15h. (c) HEA-60h. (d) Atomic percentage (at%) comparison of various elements.

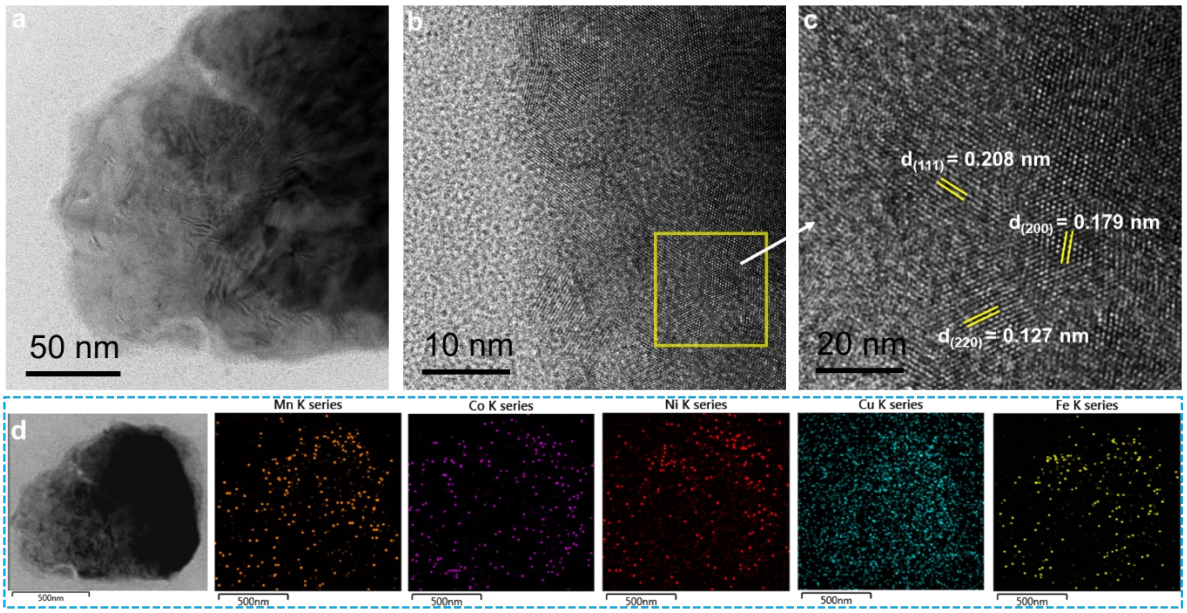

Fig. S4. Microstructural analysis of CuCoNiFeMn-HEA-60h: (a) TEM image. (b,c) HRTEM image. (d) TEM-elemental mapping images.

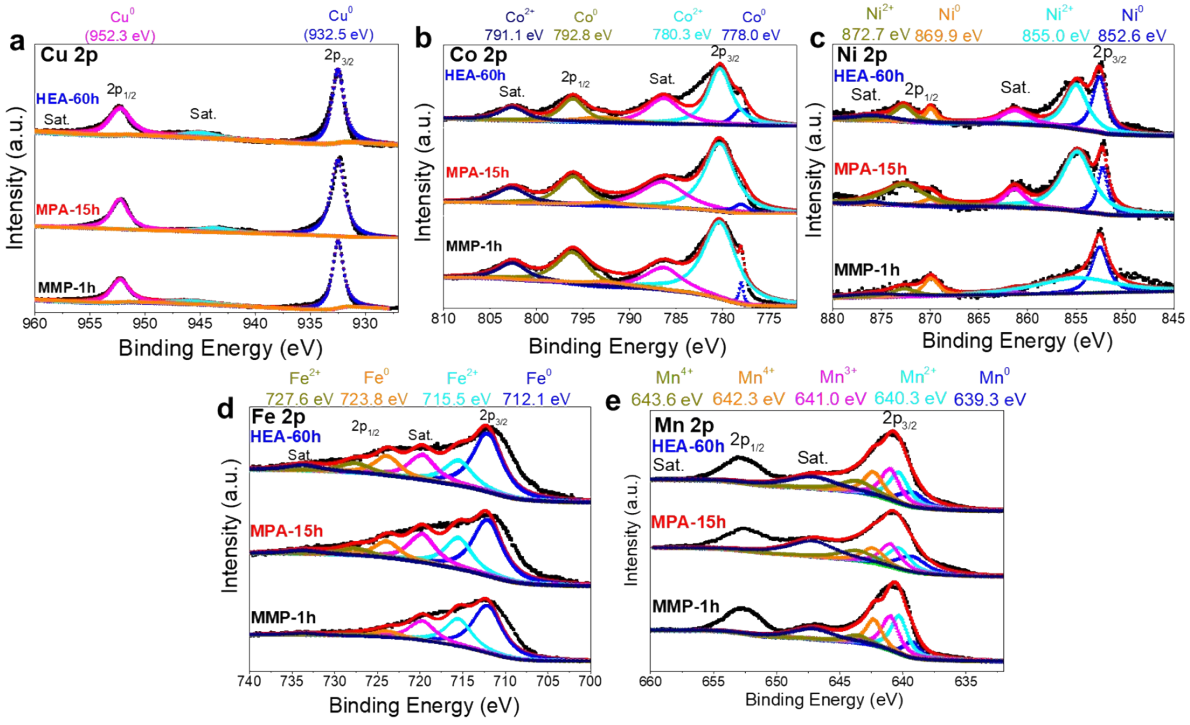

Fig. S5. Surface chemical states of HEA: Comparison of high resolution XPS spectra of (a) Cu 2p. (b) Co 2p. (c) Ni 2p. (d) Fe 2p. (e) Mn 2p.

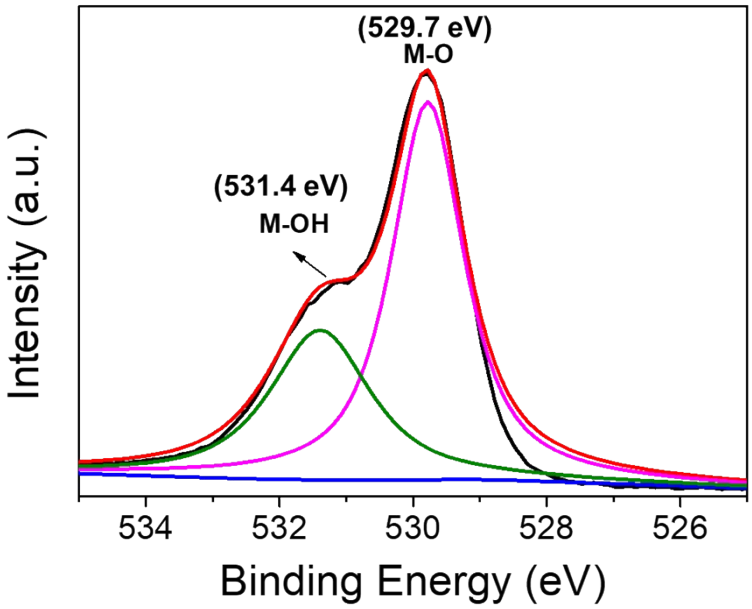

Fig. S6. XPS analysis: High-resolution O1s spectrum of CuCoNiFeMn-HEA-60h electrode.

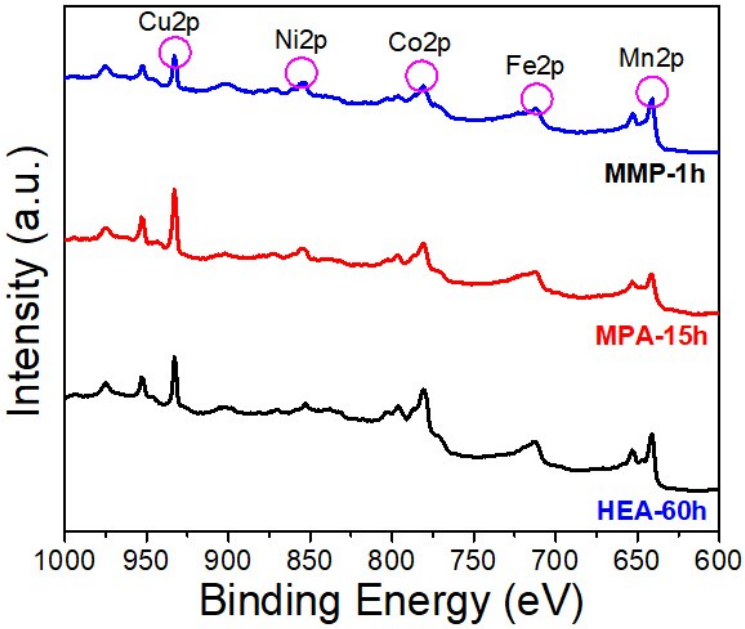

Fig. S7. XPS: Survey spectra of MMP-1h, MPA-15h and HEA-60h.

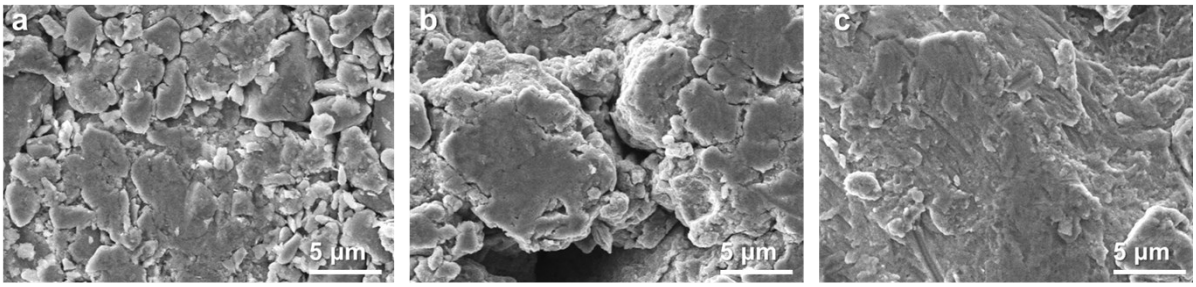

Fig. S8. SEM images: (a) MMP-1h, (b) MPA-15h and (c) HEA-60h with different grain size and boundary.

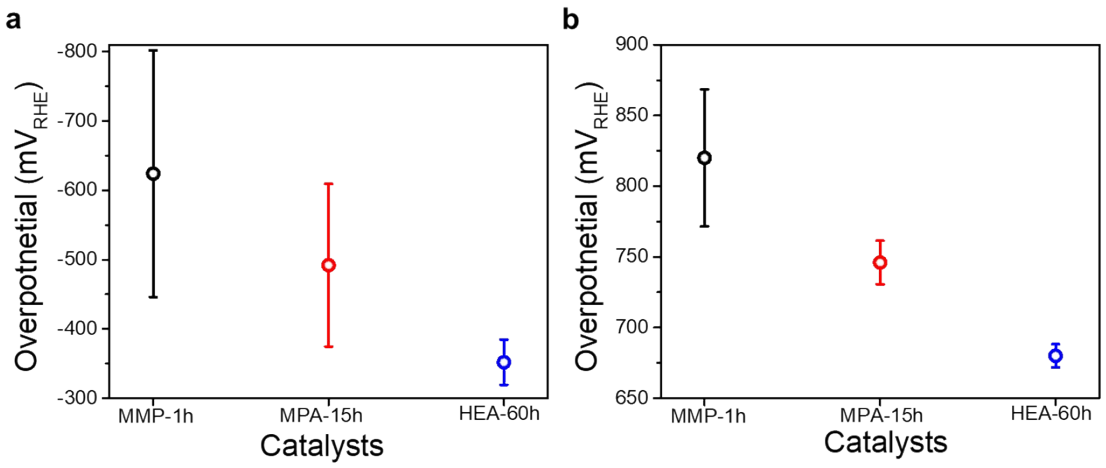

Fig. S9. Comparison of HER and OER overpotential in 1 M PBS: (a) HER overpotential at -50 mA cm^{-2}. (b) OER overpotential at 25 mA cm^{-2}. The error bars are drawn as a standard deviation using three samples.

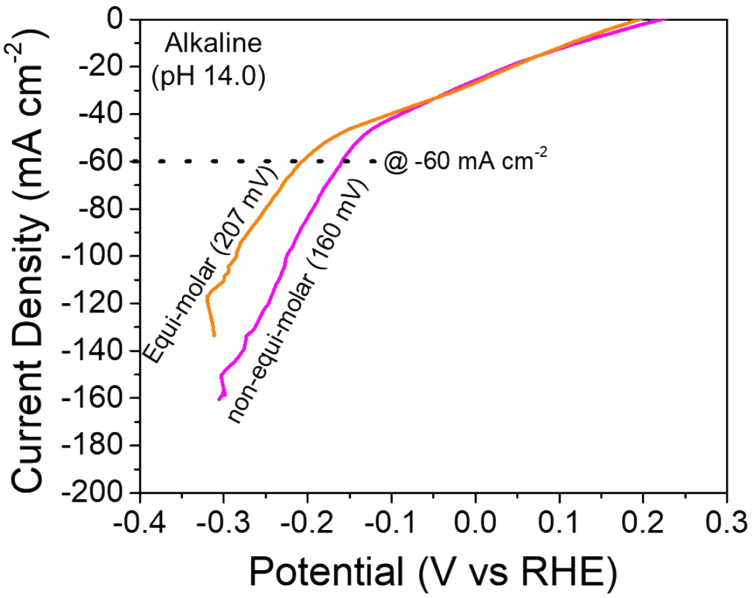

Fig. S10. Comparison of HER activity in 1 M KOH: HER-LSV (I-V curves) of equi-molar and non-equi-molar HEA systems. LSV scan rate: 10 mV s^{-1}.

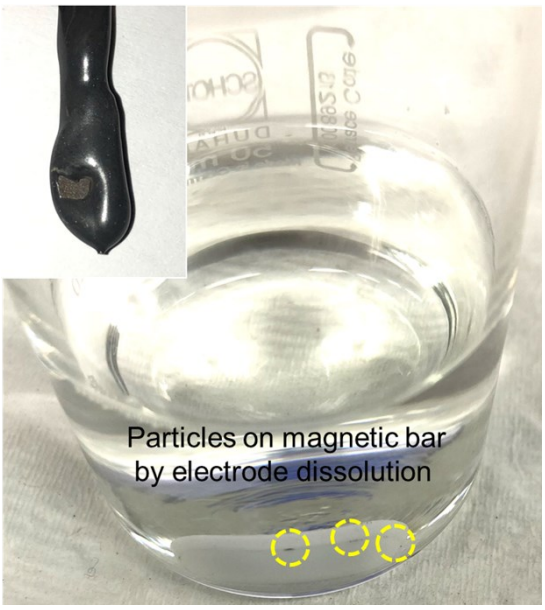

Fig. S11. Dissolution of particles from MMP-1h electrode in 1 M PBS: Particles aggregation on magnetic bar after few hours of HER stability at -50 mA cm^{-2}. Inset: electrode image.

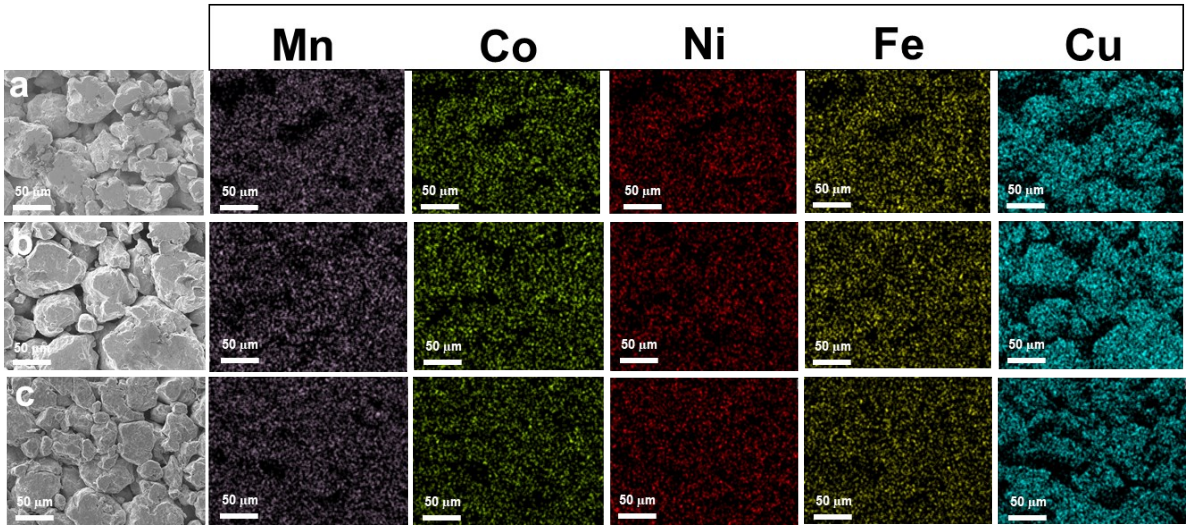

Fig. S12. Morphology and elemental mapping of HEA-60h: SEM images and distribution of elements before and after electrochemical stability test (a) before stability. (b) After HER (20h). (c) After OER (15h).

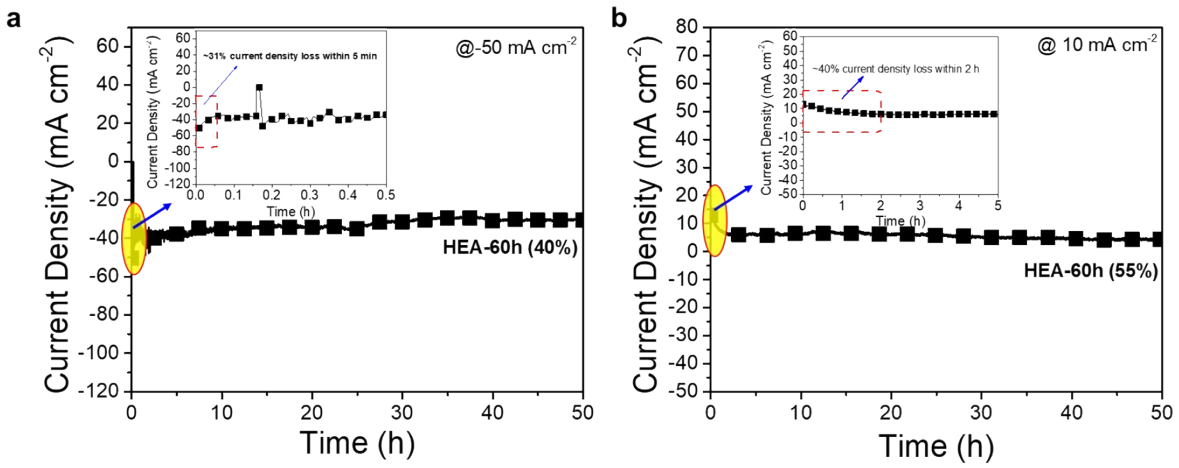

Fig. S13. Long-term HER and OER stability test of CuCoNiFeMn-HEA-60h in 1 M PBS: (a) HER stability test at a static current density of -50 mA cm^{-2}. (b) OER stability test at a static current density of 10 mA cm^{-2}.

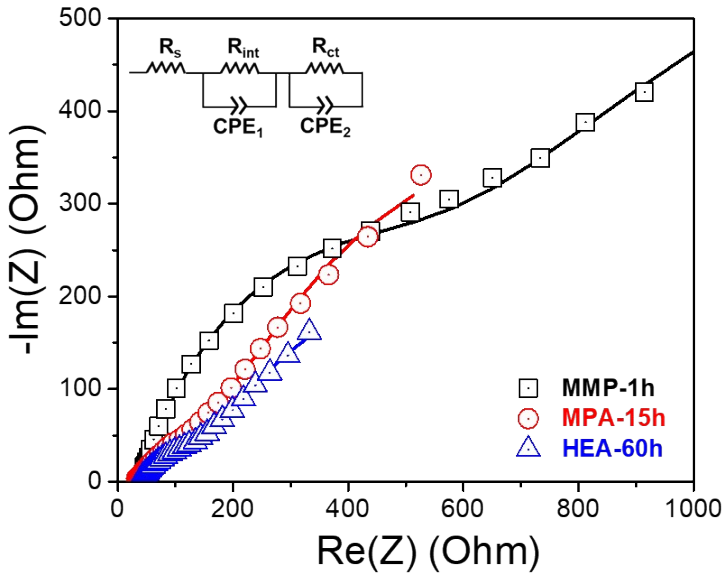

CuCoNiFeMn	R_s (Ohm)	R_{int} (Ohm)	R_{ct} (Ohm)
MMP-1h	36.5	386.3	2743
MPA-15h	28.2	311.1	885.9
HEA-60h	36.7	131.5	752.4

Fig. S14. Electrochemical impedance spectroscopy measurement of HEA in 1 M PBS: Nyquist plot (applied bias: OCV; frequency range: 7 MHz to 5 mHz). CPE –constant phase element.

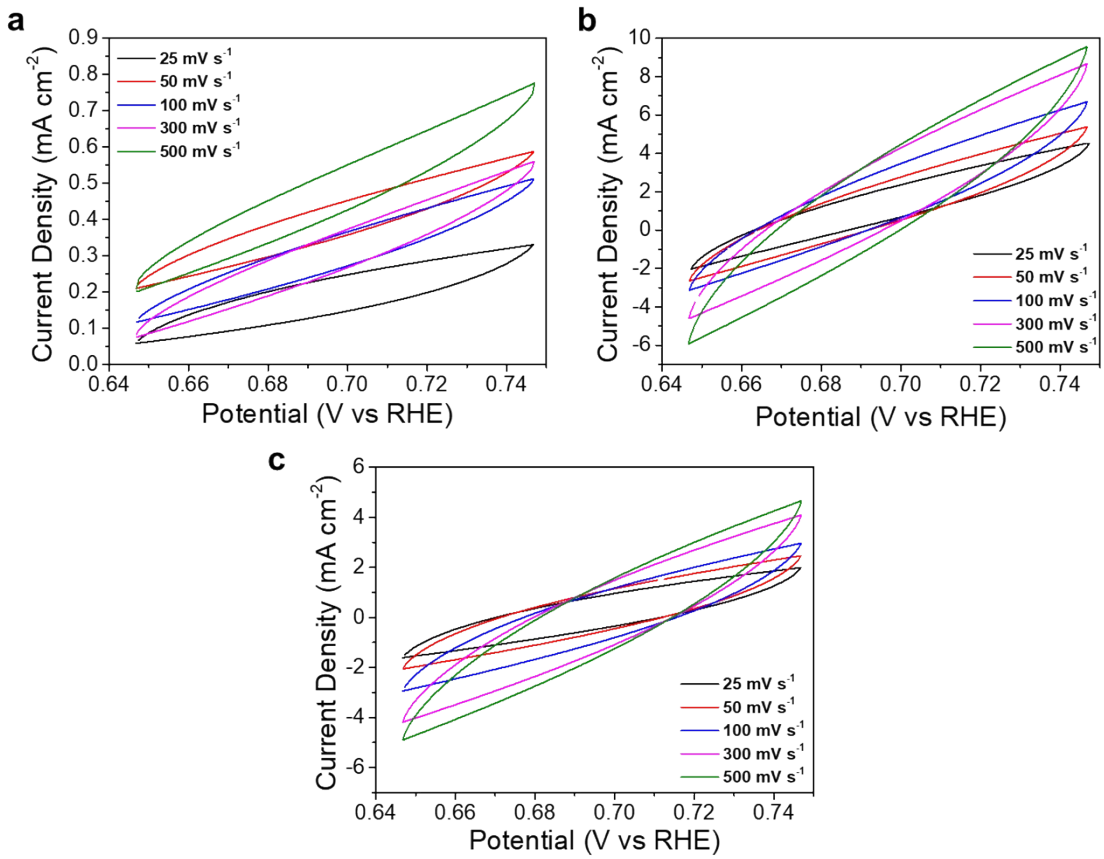

Fig. S15. Electrochemical active surface area (ESCA) in 1 M PBS: Cyclic voltammogram of (a) MMP-1h (b) MPA-15h (c) HEA-60h.

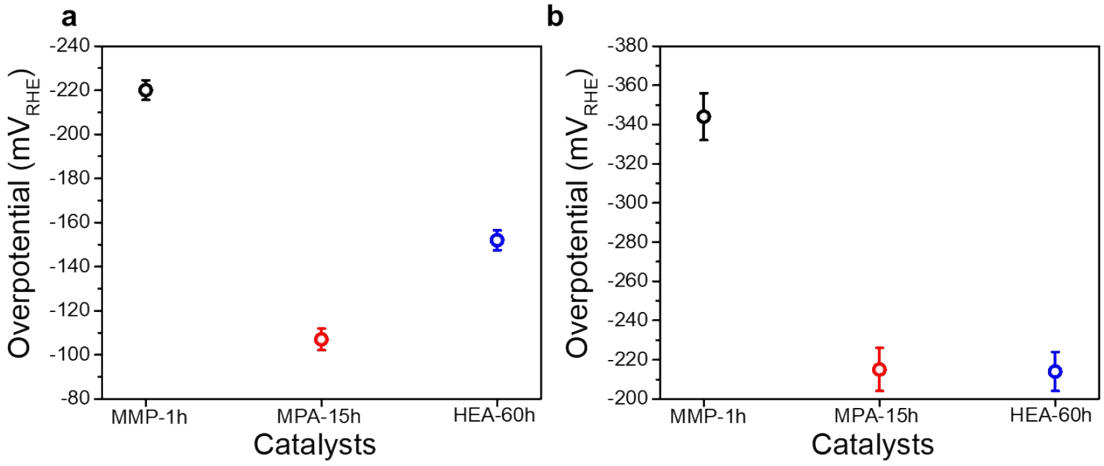

Fig. S16. Comparison of HER overpotential: (a) HER overpotential at -70 mA cm^{-2} in 1 M KOH. (b) HER overpotential at -20 mA cm^{-2} 0.5 M H_2SO_4. The error bars are drawn as a standard deviation using three samples.

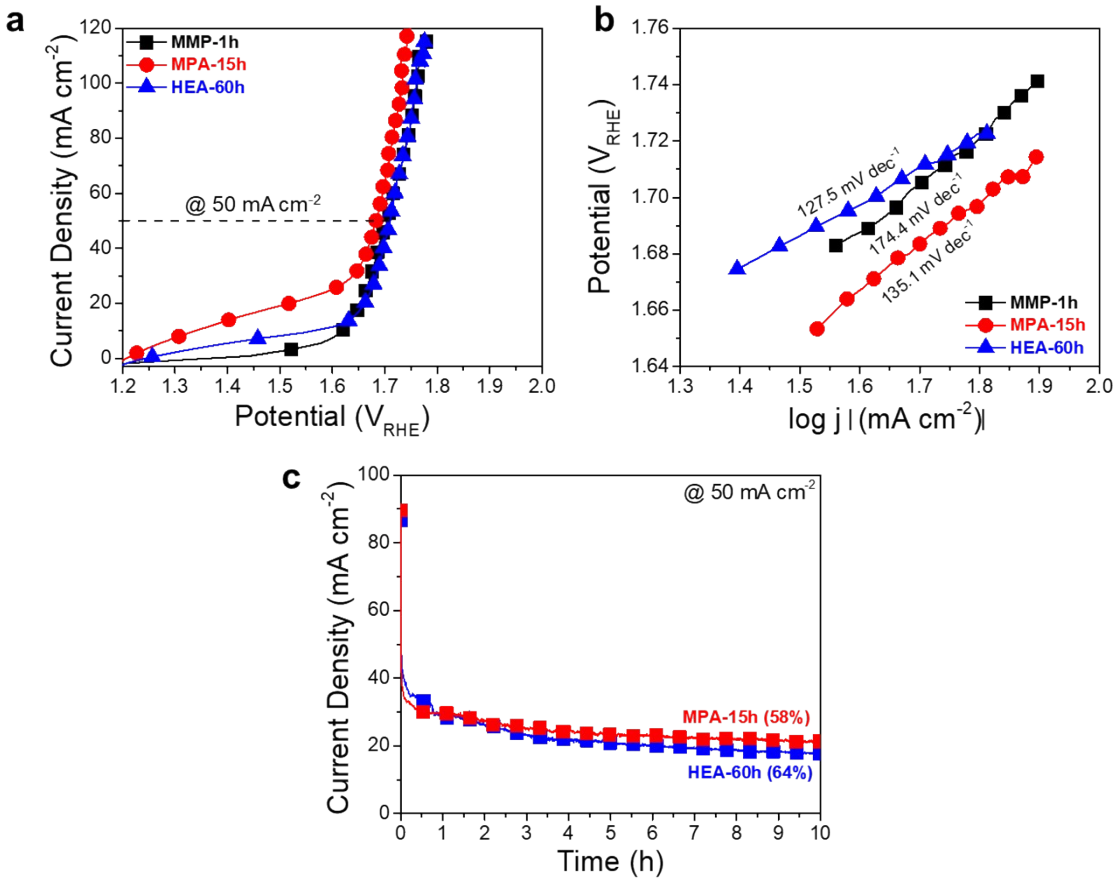

Fig. S17. Oxygen evolution activity of HEA in 1 M KOH: (a) OER-LSV (I-V curves). (b) Corresponding Tafel plot. (c) Chronoamperometry (CA, I-t curves) for 10 h at a static current density of 50 mA cm^{-2}. LSV scan rate: 10 mV s^{-1}.

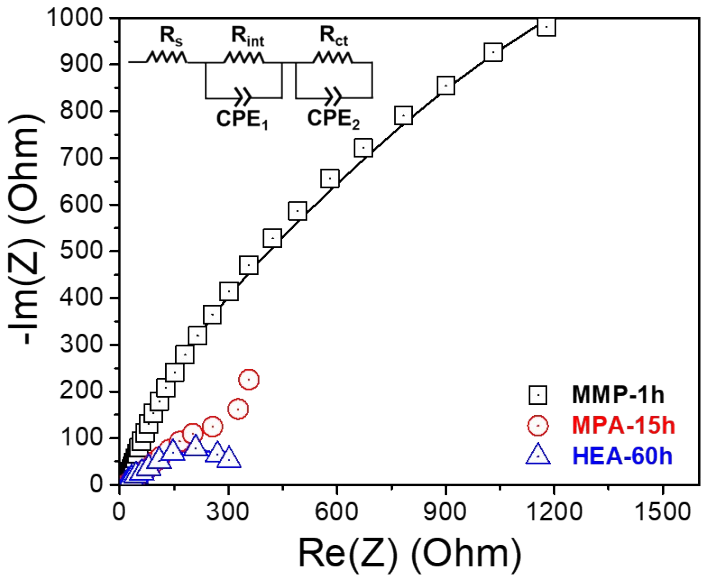

CuCoNiFeMn	R_s *(Ohm)*	R_{int} *(Ohm)*	R_{ct} *(Ohm)*
MMP-1h	17.9	347.9	3968
MPA-15h	20.3	54.81	404.6
HEA-60h	17.0	54.92	290.6

Fig. S18. Electrochemical impedance spectroscopy measurement of HEA in 1 M KOH: Nyquist plot (applied bias: OCV; frequency range: 7 MHz to 5 mHz). CPE –constant phase element.

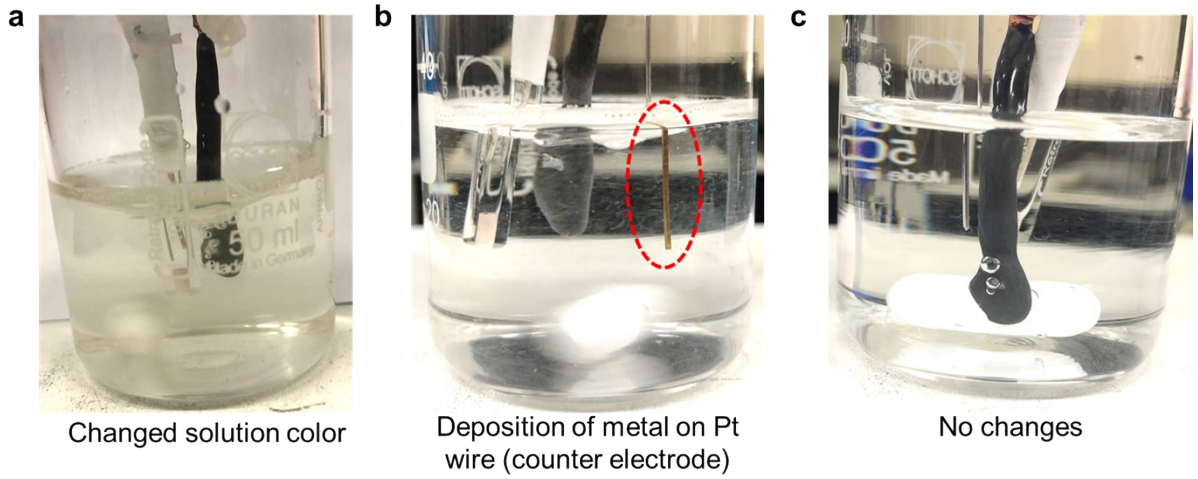

Fig. S19. Electrode digital images during HER stability in 0.5 M H_2SO_4: (a) MMP-1h. (b) MPA-15h. (c) HEA-60h at -20 mA cm^{-2} .

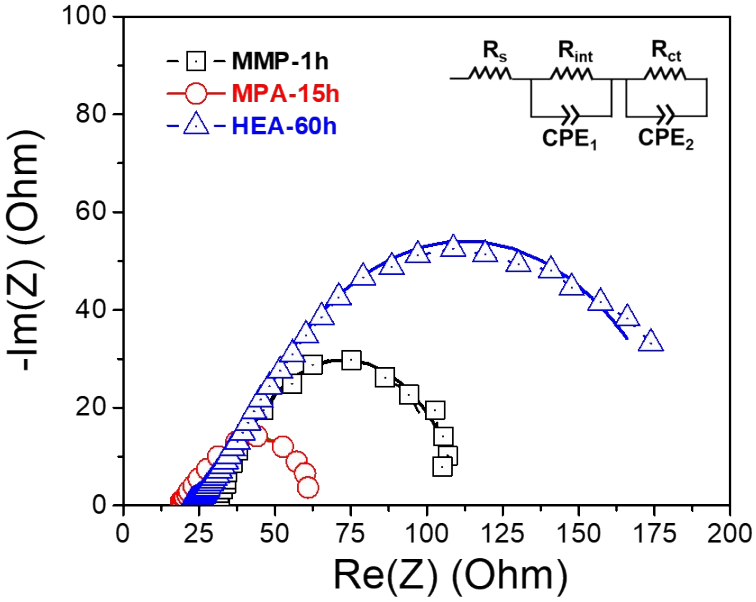

CuCoNiFeMn	R_s (Ohm)	R_{int} (Ohm)	R_{ct} (Ohm)
MMP-1h	28.5	29.2	62.0
MPA-15h	18.3	16.3	29.9
HEA-60h	22.1	40.7	131.3

Fig. S20. Electrochemical impedance spectroscopy measurement of HEA in 0.5 M H_2SO_4: Nyquist plot (applied bias: OCV; frequency range: 7 MHz to 20 mHz). CPE –constant phase element.

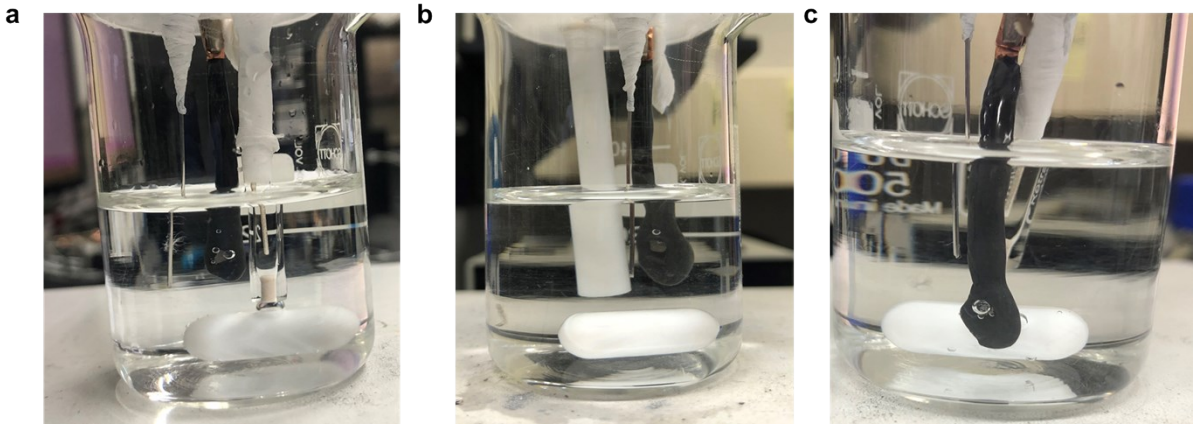

Fig. S21. Bubbles formation on electrode surface during EIS analysis in 0.5 M H_2SO_4: (a) MMP-1h. MPA-15h (c) HEA-60h.

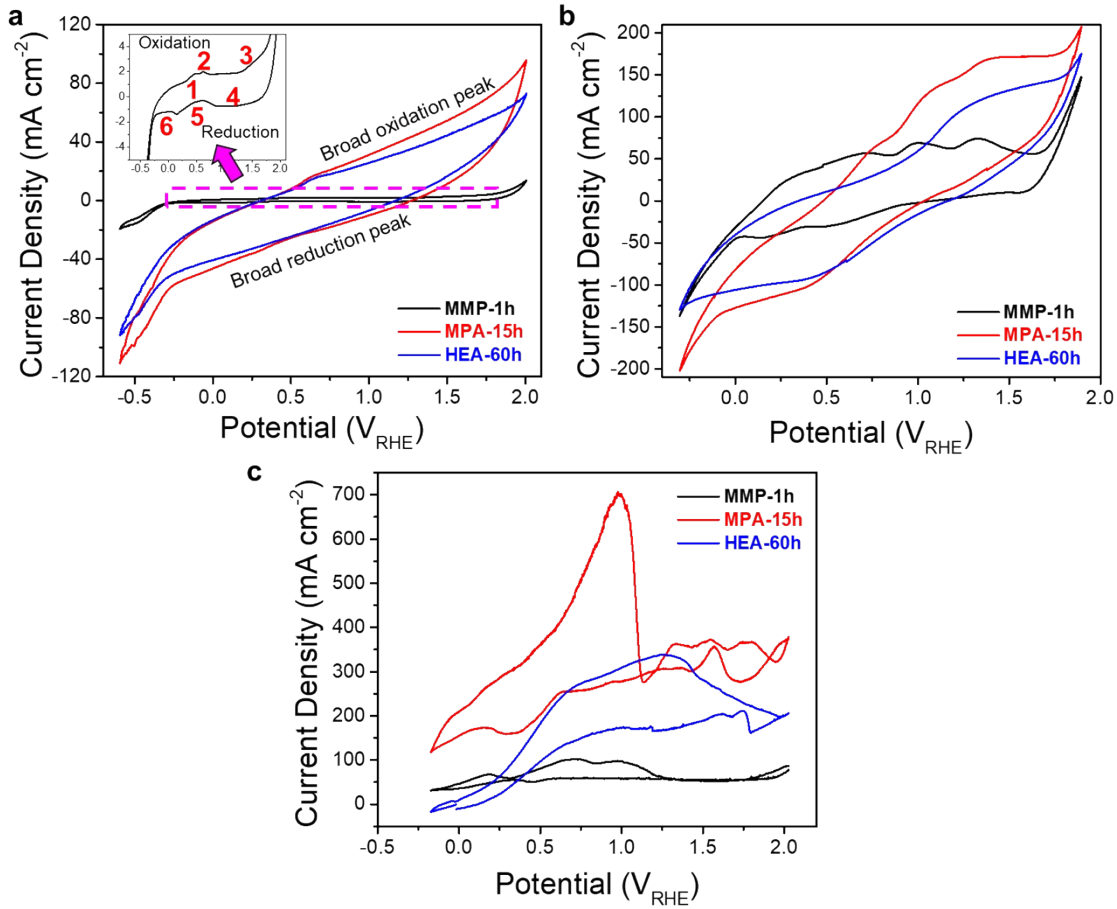

Fig. S22. Cyclic voltammetry measurements of HEA: CV curves (scan rate: 50 mV s^{-1}). of MMP-1h, MPA-15h and HEA-60h in (a) 1 MPBS. (b) 1 M KOH. (c) 0.5 M H_2SO_4.

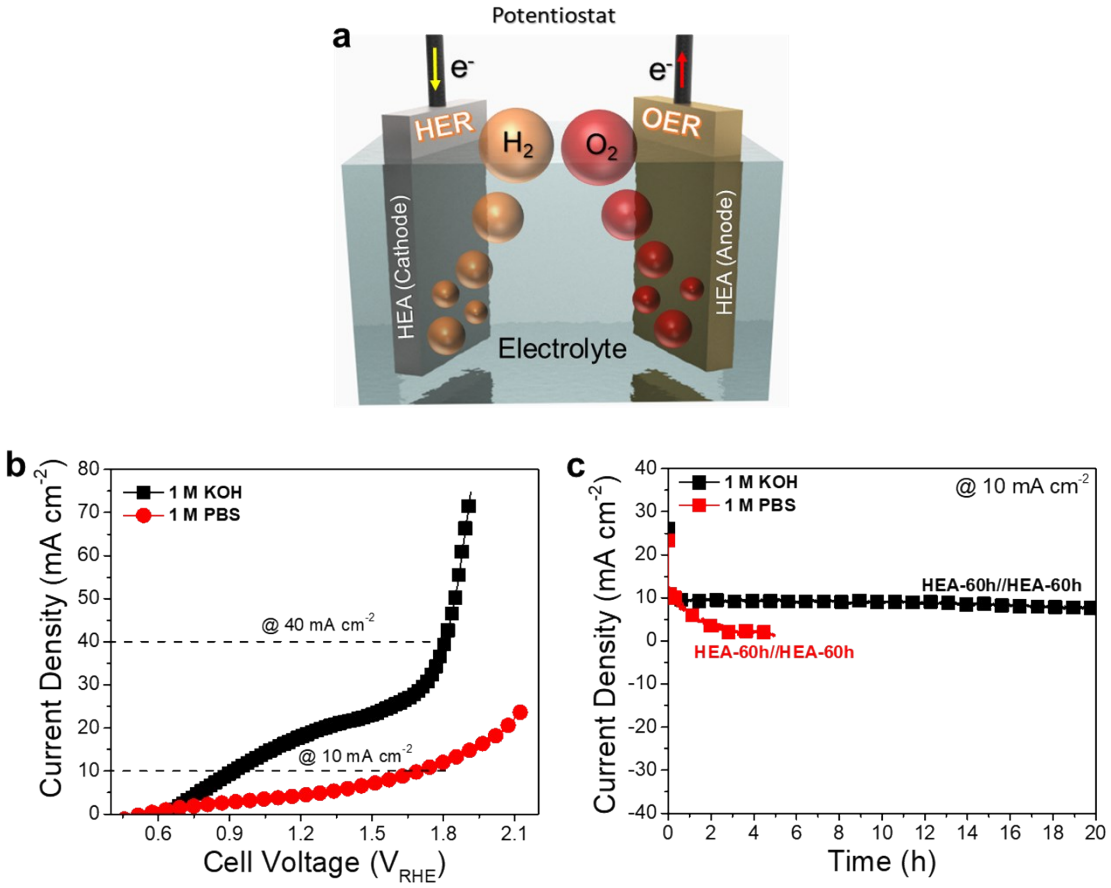

Fig. S23. Overall water splitting (two electrode system) of HEA: (a) Schematic representation of overall water splitting. (b) LSV (I-V curves) with a scan rate of 10 mV s^{-1}. (c) Chronopotentiometry (CP, I-t curves) for 20 h at a static applied current density of 10 mA cm^{-2} in 1 M KOH and PBS solution.

References

1) L. Zeng, K. Sun, Y. Chen, Z. Liu, Y. Chen, Y. Pan, R. Zhao, Y. Liu, C. Liu, Neutral-pH overall water splitting catalyzed efficiently by a hollow and porous structured ternary nickel sulfoselenide electrocatalyst, J. Mater. Chem. A. 7 (2019) 16793–16802. https://doi.org/10.1039/c9ta05601g.

2) K. Huang, B. Zhang, J. Wu, T. Zhang, D. Peng, X. Cao, Z. Zhang, Z. Li, Y. Huang, Exploring the impact of atomic lattice deformation on oxygen evolution reactions based on a sub-5 nm pure face-centred cubic high-entropy alloy electrocatalyst, J. Mater. Chem. A. 8 (2020) 11938–11947. https://doi.org/10.1039/d0ta02125c.

3) D. Wang, Z. Liu, S. Du, Y. Zhang, H. Li, Z. Xiao, W. Chen, R. Chen, Y. Wang, Y. Zou, S. Wang, Low-temperature synthesis of small-sized high-entropy oxides for water oxidation, J. Mater. Chem. A. 7 (2019) 24211–24216. https://doi.org/10.1039/c9ta08740k.

4) X. Cui, B. Zhang, C. Zeng, S. Guo, Electrocatalytic activity of high-entropy alloys toward oxygen evolution reaction, MRS Commun. 8 (2018) 1230–1235. https://doi.org/10.1557/mrc.2018.111.

5) Z. Ding, J. Bian, S. Shuang, X. Liu, Y. Hu, C. Sun, Y. Yang, High entropy intermetallic–oxide core–shell nanostructure as superb oxygen evolution reaction catalyst, Adv. Sustain. Syst. 4 (2020) 1–9. https://doi.org/10.1002/adsu.201900105.

6) H.-J. Qiu, G. Fang, J. Gao, Y. Wen, J. Lv, H. Li, G. Xie, X. Liu, S. Sun, Noble metal-free nanoporous high-entropy alloys as highly efficient electrocatalysts for oxygen evolution reaction, ACS Mater. Lett. 1 (2019) 526–533. https://doi.org/10.1021/acsmaterialslett.9b00414.

7) M.W. Glasscott, A.D. Pendergast, S. Goines, A.R. Bishop, A.T. Hoang, C. Renault, J.E. Dick, Electrosynthesis of high-entropy metallic glass nanoparticles for designer, multi-functional electrocatalysis, Nat. Commun. 10 (2019) 2650. https://doi.org/10.1038/s41467-019-10303-z.

8) W. Dai, T. Lu, Y. Pan, Novel and promising electrocatalyst for oxygen evolution reaction based on MnFeCoNi high entropy alloy, J. Power Sources. 430 (2019) 104–111. https://doi.org/10.1016/j.jpowsour.2019.05.030.

9) D. V. Franco, L.M. Da Silva, W.F. Jardima, J.F.C. Boodts, Influence of the electrolyte composition on the kinetics of the oxygen evolution reaction and ozone production processes, J. Braz. Chem. Soc. 17 (2006) 746–757. https://doi.org/10.1590/s0103-50532006000400017.

10) M. Liu, Z. Zhang, F. Okejiri, S. Yang, S. Zhou, S. Dai, Entropy-maximized synthesis of multimetallic nanoparticle catalysts via a ultrasonication-assisted wet chemistry method under ambient conditions, Adv. Mater. Interfaces. 6 (2019) 1–6. https://doi.org/10.1002/admi.201900015.

11) H. Li, Y. Han, H. Zhao, W. Qi, D. Zhang, Y. Yu, W. Cai, S. Li, J. Lai, B. Huang, L. Wang, Fast site-to-site electron transfer of high-entropy alloy nanocatalyst driving redox electrocatalysis, Nat. Commun. 11 (2020) 1–9. https://doi.org/10.1038/s41467-020-19277-9.

12) Z. Jia, T. Yang, L. Sun, Y. Zhao, W. Li, J. Luan, F. Lyu, L.C. Zhang, J.J. Kruzic, J.J. Kai, J.C. Huang, J. Lu, C.T. Liu, A novel multinary intermetallic as an active electrocatalyst for hydrogen evolution, Adv. Mater. 32 (2020). https://doi.org/10.1002/adma.202000385.